# Influence of S100A9 on Prion Protein Amyloid Aggregation

Mantas Ziaunys*, Darius Sulskis, Kamile Mikalauskaite, Andrius Sakalauskas and Vytautas Smirnovas

Institute of Biotechnology, Life Sciences Center, Vilnius University, LT-10257 Vilnius, Lithuania

*Correspondence: mantas.ziaunys@gmc.vu.lt

## Abstract

Protein aggregation in the form of amyloid fibrils has long been associated with the onset and development of various amyloidoses, including Alzheimer's, Parkinson's or prion diseases. Recent studies of their fibril formation process have revealed that amyloidogenic protein cross-interactions may impact aggregation pathways and kinetic parameters, as well as the structure of the resulting aggregates. Despite a growing number of reports exploring this type of interaction, they only cover just a small number of possible amyloidogenic protein pairings. One such pair is between two neurodegeneration-associated proteins: S100A9 and prion protein, which are known to co-localize *in vivo*. In this study, we examine their cross-interaction *in vitro* and demonstrate that S100A9 has a significant influence on not only prion protein aggregation kinetics, but also selectively promotes the formation of a specific fibril conformation.

## Introduction

Amyloid fibril formation is a key factor linked with the onset and progression of amyloidoses, including neurodegenerative Alzheimer's, Parkinson's or prion diseases [1,2]. Currently, multiple proteins and peptides of various lengths are known to aggregate into such highly organized, beta-sheet rich structures [1]. Despite countless studies and decades of research, the exact mechanism of aggregation remains enigmatic, with new potential pathways being proposed every year [3–5]. This complex nature of amyloid formation is one of the reasons why there are still very few disease modulating drugs available, with many promising candidates that show efficacy during initial studies often failing to pass clinical trials [6,7]. Considering that the sum of amyloid-related disorders is in the tens of millions and the number of affected individuals is predicted to increase even further [8,9], it is essential to decipher this process in the hopes of discovering a potential cure.

The fundamental model of amyloid aggregation consists of nucleation, elongation and two secondary processes [10]. Initially, native-state protein molecules undergo a conformation shift and associate into stable, beta-sheet rich nuclei [11,12], which then act as a catalyst for further protein incorporation, and aggregate elongation [13,14]. Once fibrils are formed, they can fragment [15] or act as a catalyzing surface for nucleation events [16,17], causing the assembly of even more aggregation centers. However, this model primarily describes single protein reactions, while the actual cell environment is densely crowded with numerous proteins and thus the aggregation mechanisms become affected by them [18]. Currently, there are multiple reports which show that amyloidogenic proteins are capable of interacting with one another, altering their aggregation pathways and resulting fibril structural characteristics. For instance, Alzheimer's disease-related amyloid beta peptide was able to influence the aggregation of multiple neurodegenerative disease-related proteins, including alpha-synuclein (Parkinson's disease) [19], Tau (Alzheimer's disease) [20,21], and prion proteins (prion diseases) [22]. Similarly, alpha-synuclein interacted

with Tau [23,24] and prion proteins [25]. Despite a growing number of such observations, the overall picture of the amyloid interactome remains incomplete.

One potential cross-interaction, which has received minimal attention, is between S100A9 and prion protein. S100A9 is part of a pro-inflammatory S100 calcium-binding protein family [26], members of which have been implicated in Alzheimer's disease, either through their association with amyloid plaques, effects on signalling pathways or interactions with amyloid beta [27]. Other studies have demonstrated their involvement with alpha-synuclein aggregation [28], as well as Tau protein hyperphosphorylation [29], suggesting that they may play an important role in the onset of amyloid disorders. Prion proteins, on the other hand, are cell-surface glycoproteins, which perform multiple physiological functions, such as copper homeostasis, neuroprotection and stem cell renewal [30]. Their amyloid aggregate formation and accumulation is associated with several disorders, including Creutzfeldt-Jakob disease, Gerstmann–Straussler–Scheinker syndrome, fatal familial insomnia [31,32] and spongiform encephalopathy [33]. According to the PAXdb Protein abundance database [34], S100A9 and prion proteins share a localization in multiple areas *in vivo*, including the cerebral cortex [35,36] and cerebrospinal fluid [37]. Both of these proteins also play roles in neuroinflammation, either by pro-inflammatory signaling of native S100A9, cytotoxicity of fibrillar S100A9 [27] or activation and proliferation of microglia by prion protein aggregates [38]. These factors, coupled with existing reports of S100A9 and prion protein cross-interactions with other amyloidogenic proteins [27,39,40], prompt the need for more in-depth investigations into this pairing.

In this work, we examined how both the non-aggregated, as well as fibrillar forms of S100A9 modulate the amyloid aggregation of a mouse prion protein fragment 89 – 230. We show that S100A9 can significantly alter the kinetic parameters of prion protein amyloid formation, as well as selectively promote the formation and self-replication of fibrils with specific secondary structures.

## Materials and Methods

### Protein aggregation assays

Mouse prion protein fragment 89-230 (further referred to as PrP) was purified as described previously [41], without the His-tag cleavage step, dialysed in 10 mM sodium acetate buffer solution for 24 hours, concentrated to 200 µM and stored at -20°C. S100A9 was purified as described in Supplementary Materials, concentrated to 300 µM in PBS buffer solution and stored at -20°C.

Thioflavin-T (ThT) was dissolved in Milli-Q $H_2O$ (~11 mM concentration) and filtered through a 0.22 µm pore size syringe filter. ThT concentration was measured by scanning a diluted dye sample's absorbance at 412 nm, using a Shimadzu UV-1800 spectrophotometer ($\varepsilon_{412}$=23250 $M^{-1}cm^{-1}$). The dye was then diluted to 10 mM and stored at -20°C under dark conditions.

To monitor PrP aggregation kinetics under various guanidine hydrochloride (GuHCl) concentrations, the PrP solution was combined with 6 M GuHCl PBS, 1x PBS, 10x PBS and 10 mM ThT solutions to yield a final protein concentration of 25 µM, 100 µM ThT, 1x PBS and 0 – 3.0 M GuHCl. The reaction solutions were then distributed to 96-well non-binding plates (100 µL volume, each well contained a 3 mm glass bead), sealed by Nunc-sealing tape and incubated at 37°C with constant 600 RPM agitation in a ClarioStar Plus plate reader. ThT fluorescence was monitored every 5 minutes using 440 nm excitation and 480 emission wavelengths.

To prepare S100A9 fibrils and monitor their formation kinetics, the S100A9 stock solution was combined with 6 M GuHCl PBS, 1x PBS and 10 mM ThT to a final protein concentration of 200 µM, 100 µM ThT and 0 or 1.5 M GuHCl. Samples, which were used to determine the residual non-aggregated S100A9 concentration at the end of the reaction, did not contain ThT (due to ThT absorbance at 280 nm). The aggregation reaction and ThT fluorescence monitoring was then conducted as in the case of PrP. For further use of S100A9 aggregates, the solutions from each well were recovered and combined. To determine the concentration of non-aggregated S100A9 in these samples, they were centrifuged at 14 000 x g for 15 minutes and the absorbance of the supernatant was measured using a Shimadzu UV-1800 spectrophotometer ($\varepsilon_{280}$ = 7100 $M^{-1}cm^{-1}$).

To monitor PrP aggregation in the presence of S100A9, the stock PrP solution was combined with either non-aggregated S100A9 or the previously prepared fibril samples, 6 M GuHCl PBS, 1x PBS, 10x PBS and 10 mM ThT. The resulting solutions contained 25 µM PrP, 100 µM ThT, 1.5 M GuHCl, 1x PBS and a range of S100A9 concentrations (0, 1, 2.5, 5, 25 and 50 µM). The aggregation reaction and ThT fluorescence monitoring was then conducted as in both other previously described cases.

All reaction lag time and apparent rate constant values were determined as described previously [39]. In brief, each sigmoidal curve was fit using a Boltzmann sigmoidal equation and lag time, apparent rate constants were determined from the fit parameters. For seeded aggregation, the reaction $t_{50}$ values were determined by normalizing the curves between 0 and 1 and applying a linear fit between 0.4 and 0.6 intensity value data points. The time point at 0.5 value of the linear fit Y-axis was regarded as the reaction's $t_{50}$ value. All data analysis was done using Origin software.

**Prion protein self-replication**

To prepare PrP samples for Fourier-transform infrared spectroscopy, aliquots of each PrP aggregate sample (40 µL) were combined with the initial reaction solution (360 µL, which did not contain S100A9) and incubated under identical conditions as were used in the initial kinetic monitoring assay. This procedure was repeated twice to reduce the concentration of S100A9 in the solution.

To measure PrP self-replication in the presence of S100A9, 60 µL aliquots of PrP fibrils (prepared in the absence of S100A9) were combined with the initial reaction solutions (540 µL), which were supplemented with either non-aggregated S100A9 or S100A9 fibrils. The final reaction solutions contained 25 µM PrP, 0 – 50 µM S100A9, 100 µM ThT, 1.5 M GuHCl and 1x PBS. Aggregation monitoring was done as in previous cases.

**Aggregate stability against denaturation**

The prepared S100A9 aggregate samples were combined with 1x PBS and 6 M GuHCl PBS, resulting in solutions with 40 µM S100A9 and a range of GuHCl concentrations (0 – 4.5 M with 0.1 M increments). The solutions were then distributed to 200 µL test-tubes and incubated at 37°C for 24 hours without agitation. After incubation, they were distributed to 96-well non-binding plates (100 µL volume in each well) and their optical densities at 600 nm ($OD_{600}$) were scanned using a ClarioStar Plus plate reader. The optical density values were corrected by subtracting the $OD_{600}$ values of control solutions, which did not contain S100A9.

**Fourier-transform infrared spectroscopy (FTIR)**

200 µL aliquots of each sample were centrifuged at 14 000 x g for 15 minutes, after which the supernatant was carefully removed and replaced with 200 µL of $D_2O$, containing 400 mM NaCl [42]. The centrifugation and resuspension procedure was repeated 4 times. The resulting sample FTIR spectra were acquired as previously described [43], using a Bruker Invenio S FTIR spectrometer. The spectra were baseline corrected and normalised to the same band area in the range between 1595 $cm^{-1}$ and 1700 $cm^{-1}$. Spectra deconvolution was done as described previously [43], using a Gaussian peak-fitting function, number of peaks – 4, RMS noise – 0.04. Data processing was done using GRAMS software.

**Atomic force microscopy**

40 µL aliquots of samples were placed on freshly cleaved mica, incubated for 2 minutes at room temperature, washed with 2 mL of Milli-Q $H_2O$ and dried using airflow. The AFM image acquisition was done as described previously [43], using a Bruker Dimension Icon atomic force microscope. 1024 x 1024 pixel resolution images were flattened using Gwyddion 2.57 software. Fibril cross-sectional heights were determined by tracing lines perpendicular to the fibril axes (n=30).

**Protein melt assay**

8-Anilinonaphthalene-1-sulfonic acid (ANS) was dissolved in Milli-Q $H_2O$ (~6 mM concentration) under dark conditions and filtered through a 0.22 µm pore size syringe filter. ANS concentration was measured by scanning a diluted dye sample's absorbance at 351 nm, using a Shimadzu UV-1800 spectrophotometer ($\varepsilon_{351}$=5500 $M^{-1}cm^{-1}$). The dye was diluted to 5 mM and used immediately after preparation. PrP and S100A9 stock solutions were combined with 1x PBS and 5 mM ANS to final protein concentrations of 100 µM and 100 µM ANS. The samples were then placed in 3 mm pathlength quartz cuvettes (200 µL volume, sealed with a plug cap) and ANS fluorescence was measured using a Varian Cary Eclipse spectrofluorometer. The protein melt assay was conducted by incubating the samples at 25°C for 5 minutes, followed by a gradual temperature increase of 2°C/min. Measurements were taken every 30 seconds, using 370 nm excitation and 470 emission wavelengths, 2.5 s signal averaging time. For each condition, the protein melt assay was repeated 3 times. The protein melting point temperature ($T_m$) values were compared by calculating the first derivative of the fluorescence curves (10 point Savitzky-Golay smoothing) and determining their maximum value positions.

**Size-exclusion chromatography**

Size exclusion chromatography (SEC) was performed with a Tricorn 10/300 column loaded with Superdex 75 resin (Cytiva) on ÄKTA start protein purification system (Cytiva) at 4 °C. The column was equilibrated with PBS buffer supplemented with 1.5 M GuHCl. Approximately 250 µL samples containing 100 µM of S100A9, PrP or a mixture of both were injected into a column.

## Results

In order to examine how both the non-aggregated and amyloid fibril forms of S100A9 influence the aggregation process of mouse prion protein 89-230 (PrP), it was first necessary to determine suitable experimental conditions. In an ideal case, meeting three key criteria was essential for obtaining reliable results: a) the prion protein aggregation reaction concludes in a reasonable timeframe (to avoid gradual

sample evaporation and fluorescent dye hydroxylation [44]), b) the generated S100A9 fibrils remain stable under the selected conditions, c) the spontaneous aggregation of S100A9 is significantly hindered. Since prion protein aggregation *in vitro* is often conducted under denaturing conditions, adjustment of this factor was chosen as a basis for achieving all three criteria.

PrP aggregation under a range of guanidine hydrochloride (GuHCl) concentrations (Figure 1A) revealed that the shortest lag time for PrP fibril formation was around 2.2 M (100 – 150 minutes). Both lower and higher denaturant concentrations resulted in substantially longer time periods (1300 – 1500 minutes at 1 M GuHCl and 250 – 300 minutes at 3 M GuHCl). In the case of 1.0 – 1.2 M GuHCl, the aggregation was also significantly more stochastic with larger deviations in lag time values. Based on these results, suitable GuHCl concentrations for PrP – S100A9 coaggregation studies would range from 1.4 M to 3.0 M.

Next, it was determined under which denaturant conditions S100A9 amyloid fibrils would remain stable for extended periods of time. For this reason, S100A9 aggregates (prepared in PBS at 37°C, 200 µM protein concentration) were combined with a range of different GuHCl concentration solutions and incubated at 37°C for 24 hours. The resulting solution optical densities (Figure 1B) were similar to the control samples up to 1.5 M, indicating the fibrils remain stable under these conditions. However, beyond 1.5 M, the optical density decreased and reached a plateau at ~3.0 M GuHCl, suggesting dissociation of fibrils. Fitting the data with a Boltzmann sigmoidal equation revealed that the denaturation midpoint was at 2.2 M. Based on both of these assays, it was evident that a GuHCl concentration of 1.5 M would be a suitable intermediate point between a rapid onset of prion protein aggregation and the stability of S100A9 fibrils.

To examine how such a denaturant concentration would influence the aggregation process of native S100A9, its fibril formation kinetics were monitored under both 0 M and 1.5 M GuHCl conditions (Figure 1C). Without GuHCl, the aggregation of 200 µM S100A9 proceeded quickly with only a short lag phase and there was an overall 10-fold increase in thioflavin-T (ThT) fluorescence. In the presence of 1.5 M GuHCl, the fluorescence intensity value was significantly smaller, and the signal experienced a long, gradual increase over the entire monitoring period. Since ThT fluorescence intensity can be modulated by different solution ionic strength values, it can not be directly compared between conditions. For this reason, the concentration of aggregated S100A9 was determined as described in the Materials and Methods section. Both 0 M and 1.5 M GuHCl conditions resulted in residual, non-aggregated protein, however, its concentration was significantly higher in the case of 1.5 M GuHCl (~65 µM, as opposed to ~23 µM out of the initial 200 µM). At lower S100A9 concentration (50 µM) and under 1.5 M GuHCl conditions, there were no detectable signs of ThT fluorescence increase during this time period and the concentrations of non-aggregated S100A9 remained similar to its initial reaction solution (Figure 1C). These results displayed that such conditions would be suitable to maintain S100A9 in its non-aggregated state for the duration of the experiments with PrP amyloid formation.

Since prolonged incubation times under conditions with GuHCl may induce a certain level of structural or morphological alterations, both samples, where S100A9 fibrils were incubated or prepared at 1.5 M GuHCl, were examined using Fourier-transform infrared spectroscopy (FTIR, Figure 1D), as well as atomic force microscopy (AFM, Figure 1E, F). In the case of S100A9 fibrils prepared without GuHCl and then incubated with the denaturant, the FTIR spectrum retained a high level of similarity to the control (control did not change during incubation without GuHCl), with an identical main maximum position (1618 $cm^{-1}$, related to strong beta-sheet hydrogen bonding [45]) and a slightly lower ratio between the

main maximum position and 1650 $cm^{-1}$ (related to random-coil or alpha-helix hydrogen bonding). This suggests that, for the most part, S100A9 fibrils were capable of retaining their original secondary structure. For S100A9 aggregates which were prepared under the 1.5 M GuHCl conditions, the main maximum was shifted towards 1619 $cm^{-1}$, the 1618 $cm^{-1}$ / 1650 $cm^{-1}$ ratio was lower than both the control and the incubated fibril spectra ratios and the small peak associated with anti-parallel beta-sheets (1692 $cm^{-1}$) was slightly shifted towards a higher wavenumber. Deconvolution of all three spectra confirmed that incubation of S100A9 fibrils at 1.5 M GuHCl had a lower effect on the reduction of beta-sheet content than when S100A9 aggregation was conducted under the same conditions (Supplementary Figure S1).

Analysis of both samples with AFM revealed that they also had distinct morphological characteristics. Both types of aggregates possessed the appearance of short, worm-like structures, which have been reported in previous studies [46]. However, the fibrils prepared at 1.5 M GuHCl had a significantly higher average cross-sectional height distribution (Figure 1G, n=50, $p<0.001$).

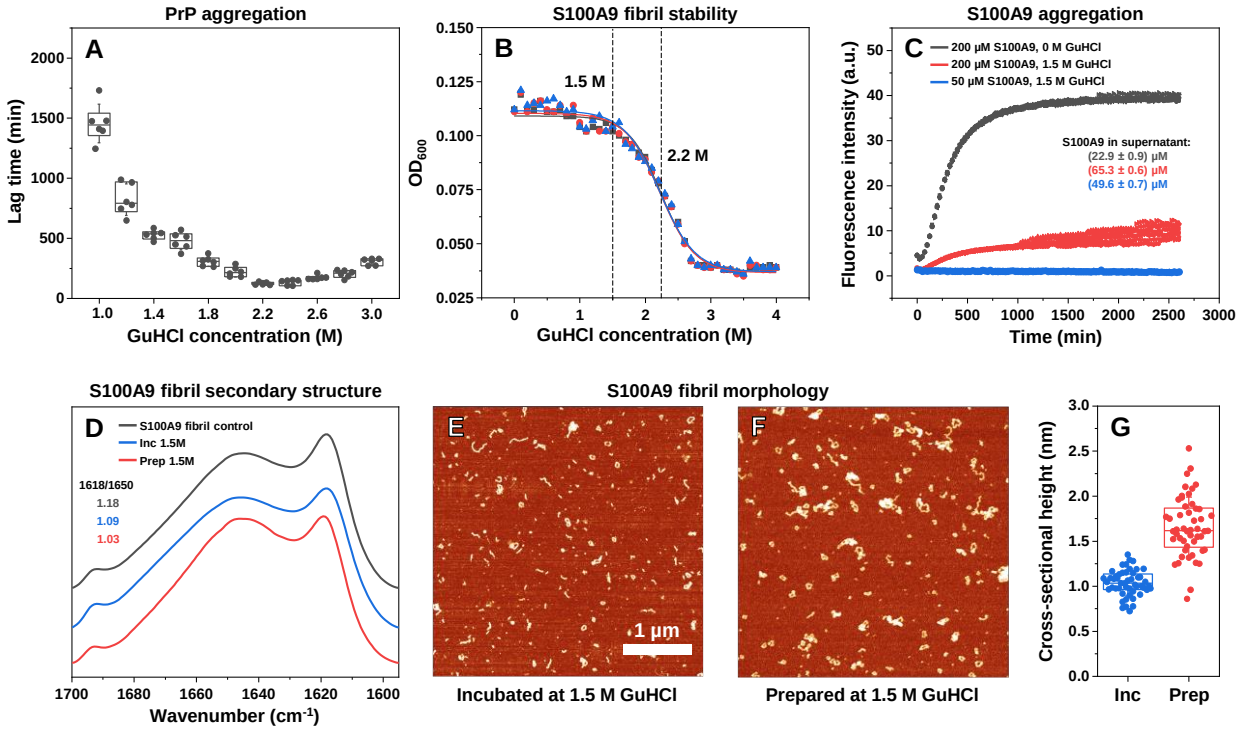


**Figure 1.** Influence of guanidinium hydrochloride (GuHCl) concentration on prion protein and S100A9 aggregate formation. PrP aggregation lag time (n=6) dependence on GuHCl concentration (A). Optical density of S100A9 fibril samples (n=3) under a range of GuHCl concentrations (B). Aggregation kinetics of S100A9 (n=4) under 0 M and 1.5 M GuHCl conditions (C). Fourier-transform infrared spectra of S100A9 aggregates prepared and incubated under 0 M (control) and 1.5 M GuHCl conditions (D). Atomic force microscopy images of S100A9 aggregates incubated (E) and prepared (F) under 1.5 M GuHCl conditions and their cross-sectional height distribution (G, n=30). Error bars are for one standard deviation, box plots indicate the interquartile range.

Considering that the selected 1.5 M GuHCl conditions yielded relatively quick aggregation of PrP, maintained the stability of preformed S100A9 fibrils and inhibited the aggregation of native S100A9, they

were selected for further cross-interaction experiments. Due to the statistically significant difference of S100A9 aggregates prepared under 1.5 M GuHCl conditions, they were also analysed alongside the 0 M GuHCl fibrils and non-aggregated S100A9.

To examine how the presence of S100A9 affects the aggregation of PrP, a range of non-aggregated and fibrillar S100A9 concentrations were combined with 25 µM prion protein and the fibril formation reaction was tracked in the presence of 1.5 M GuHCl, 600 RPM orbital agitation and a constant 37°C temperature. All statistical analysis was done using an ANOVA Bonferroni means comparison ($n=16$, $p<0.001$). When PrP was in the presence of non-aggregated S100A9, no statistically significant differences were observed at 1 µM, 2.5 µM and 5 µM protein concentrations, despite a slow and gradual increase in the process lag time values (Figure 2A, Supplementary Figure S2). Higher S100A9 concentrations, however, led to a significant increase in lag time when compared to the control and lower protein concentrations, with 25 µM conditions having an average value of 1140 minutes and 50 µM – 1760 minutes. Opposite to the effect of non-aggregated S100A9, the entire concentration range of its aggregated forms, prepared under 0 M GuHCl (Figure 2B) did not cause statistically significant deviations from the control sample lag time values. Similar results were also obtained when using S100A9 fibrils, which were prepared under 1.5 M GuHCl conditions (Figure 2C).

Contrary to the influence that non-aggregated S100A9 had on the lag time of PrP aggregation, it did not cause significant changes to the reaction's apparent rate constant (Figure 2D). However, there was a notable reduction in the process stochasticity, with 5, 25 and 50 µM concentrations leading to a reduced variation in the apparent rate constant. In the case of S100A9 fibrils prepared under 0 M GuHCl conditions, only the highest S100A9 concentration yielded apparent rate values that were significantly higher than the control (Figure 2E). A peculiar aspect was observed for the 5 µM S100A9 concentration, where it pertained a relatively low level of stochasticity when using all three forms of S100A9. The 1.5 M GuHCl S100A9 aggregates did not have such a profound effect, which may be related to either their different structure or the presence of a substantial concentration of non-aggregated S100A9 (Figure 2F).

Finally, it was investigated how the presence of S100A9 modulated PrP aggregate ThT-binding properties and fluorescence of the samples, as these parameters may be indicative of different PrP fibril strain formation [47]. When using non-aggregated S100A9, only the 50 µM concentration conditions yielded a significantly lower average fluorescence signal intensity, while all other conditions remained similar to the control (Supplementary Figure S3A). S100A9 aggregated under 0 M GuHCl conditions, on the other hand, had significantly diminished the fluorescence intensities under 1, 2.5 and 5 µM concentrations (Supplementary Figure S3B). Interestingly, the 25 and 50 µM concentrations resulted in aggregates with similar values as the control, albeit with a massively reduced stochasticity. As was the case with the apparent rate constant results, the 1.5 M GuHCl S100A9 fibrils led to an intermediate variant of intensity values, with part of them being similar to the non-aggregated S100A9 and others – to the 0 M S100A9 fibril conditions (Supplementary Figure S3C). Unlike the 0 M GuHCl aggregates, the high level of stochasticity for most of the conditions yielded no statistically significant deviations from the control. One notable observation was the highly reduced stochasticity of the 50 µM S100A9 sample fluorescence intensities when using all three forms of S100A9, similar to the case of the apparent rate constant at 5 µM protein concentration.

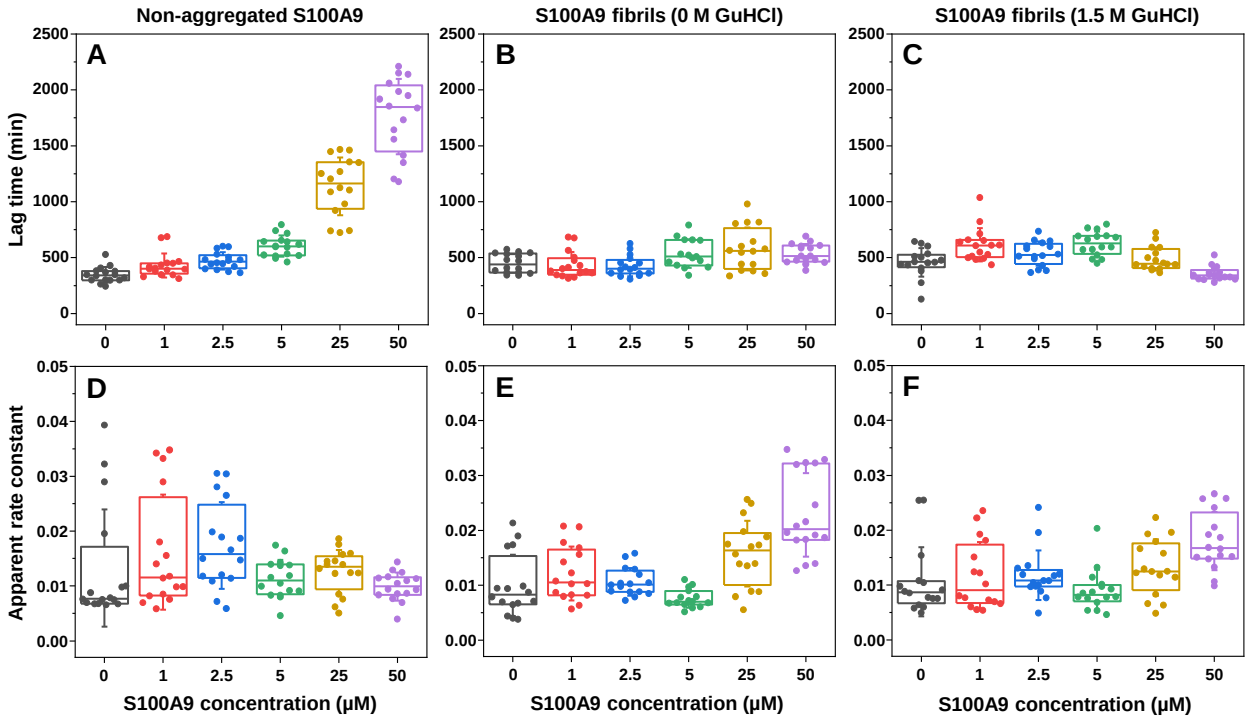


**Figure 2.** PrP aggregation kinetic parameters in the presence of different S100A9 concentrations. The lag time (A – C) and apparent rate constant (C – F) distributions of prion protein aggregation in the presence of non-aggregated S100A9 (first column), S100A9 fibrils prepared under 0 M GuHCl (second column) and 1.5 M conditions (third column). All data points are colour-coded, error bars are for one standard deviation (n=16) and box plots indicate the interquartile range.

To further explore the influence of S100A9 on the secondary structure of PrP aggregates, the resulting samples were examined using Fourier-transform infrared (FTIR) spectroscopy. Since most of them contained both PrP and S100A9, the samples were subjected to two rounds of reseeding, where aliquots of each sample (40 µL) were combined with the initial aggregation solution (360 µL, which did not contain S100A9) and incubated under identical conditions as were used in the initial kinetic monitoring assay. This procedure was done to reduce the concentration of S100A9 in the sample to negligible levels, determine if the PrP aggregates are capable of self-replication and to increase their quantity for further analysis. Taking into consideration that both the 0 M and 1.5 M GuHCl condition S100A9 fibrils displayed a similar influence on PrP aggregation kinetic parameters, only the 0 M condition samples were analysed in the FTIR assay.

Since prion protein aggregation has an intrinsic property of generating fibrils with varying secondary structures [47], all 16 FTIR spectra and their second derivatives from each condition were superimposed and the dominant types were used for comparison. The FTIR spectra of the control samples (Figure 3A) had main maxima positions at 1627 – 1628 $cm^{-1}$ and their second derivatives (Figure 3F) displayed minima at 1611 $cm^{-1}$ and 1627 $cm^{-1}$, suggesting two types of hydrogen bonding in the beta-sheet structure. The second derivatives also contained minima at 1647 $cm^{-1}$ (alpha-helix or random coils), as well as 1659, 1668 and 1677 $cm^{-1}$ (turn/loop motifs). Similar PrP aggregates were observed and analysed in our previous amyloid protein cross-interaction study [39]. Spectra of samples with an initial 5 µM non-

aggregated S100A9 were identical (Figure 3B, G), with similar minima positions as the control samples (Figure 3 table insert). In the case of 5 µM S100A9 fibrils, however, the dominant PrP FTIR spectra second derivatives (Figure 3H) displayed two minima at 1616 and 1628 $cm^{-1}$, suggesting the formation of different strength beta-sheet hydrogen bonding.

When 50 µM of S100A9 was present during the aggregation of PrP, both their forms induced the formation of a different type of PrP amyloid structure. The resulting FTIR spectra (Figure 3D, E) main maxima were shifted to 1626 $cm^{-1}$, while the second derivatives (Figure 3I, J) contained minima at 1614, 1629 and 1643 $cm^{-1}$ (associated with three different strength hydrogen bonds in the beta-sheet structure). The second derivatives also did not contain a minimum at ~1650, implying a lower amount of alpha-helical or random-coil regions. The positions associated with turn/loop motifs remained fairly similar to the control and 5 µM S100A9 condition spectra. Interestingly, the spectra observed at the highest S100A9 concentration conditions was almost identical to the one determined in a previous amyloid protein interaction study involving PrP and superoxide dismutase-1 (SOD1), where this type of aggregate was among two other PrP fibrils formed in the presence of 25 µM SOD1 [39].

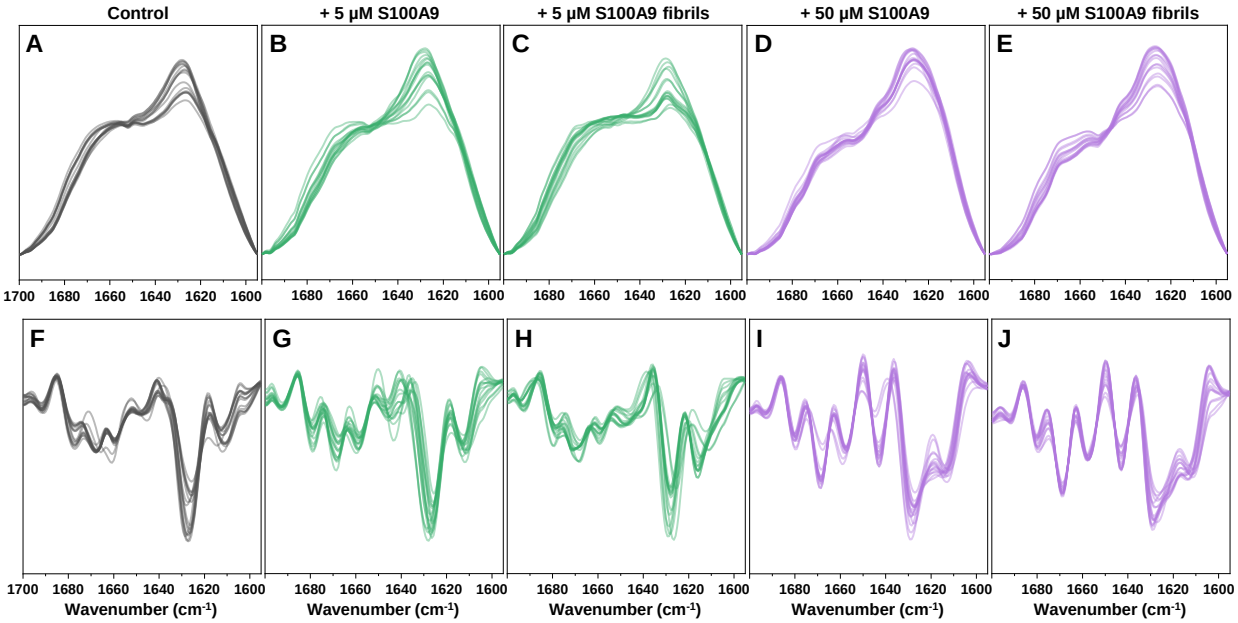


| 25 µM PrP with: | Beta-sheet | Alpha-helix Random-coil | Turn/Loop |
|---|---|---|---|
| Control | 1611/1627 | 1647 | 1659/1668/1677 |
| 5 µM S100A9 | 1612/1627 | 1646 | 1659/1668/1679 |
| 5 µM S100A9 fibrils | 1616/1628 | 1649 | 1659/1668/1678 |
| 50 µM S100A9 | 1614/1629/1643 | - | 1658/1668/1680 |
| 50 µM S100A9 fibrils | 1614/1629/1643 | - | 1658/1668/1680 |

**Figure 3.** Secondary structure comparison of PrP fibrils formed in the presence of different S100A9 concentrations. The FTIR spectra of the control (A), 5 µM non-aggregated S100A9 (B), 5 µM S100A9 fibril (C), 50 µM non-aggregated S100A9 (D) and 50 µM S100A9 fibril (E) condition PrP fibrils and their second derivatives (F – J). Table insert displays the dominant spectra second derivative minima positions related to beta-sheet, alpha-helix, random-coil and turn/loop hydrogen bonding.

Since the presence of S100A9 had a significant effect on PrP spontaneous aggregation kinetics and the resulting fibril secondary structure, it was further investigated whether S100A9 also affected their self-

replication properties. Different concentrations of non-aggregated and fibrillar S100A9 were incubated with the initial prion protein reaction solutions, containing 10% of PrP fibrils. In the absence of S100A9, the reaction proceeded without a lag phase and the average aggregation half-time value ($t_{50}$) was 160 minutes (Figure 4). The presence of S100A9 resulted in sigmoidal aggregation curves with higher $t_{50}$ values, suggesting that it may be capable of inhibiting the self-replication properties of PrP fibrils. In the case of non-aggregated S100A9 (Figure 4A), there was a concentration-dependent increase in $t_{50}$ values up to 40 µM (Figure 4C). Oppositely, the inhibitory effect became saturated at only 20 µM of S100A9 fibrils (Figure 4B, C). A comparison of PrP aggregation half-time values in the presence of 50 µM S100A9 (Figure 4C) revealed that the inhibition was higher when S100A9 was in its non-aggregated state.

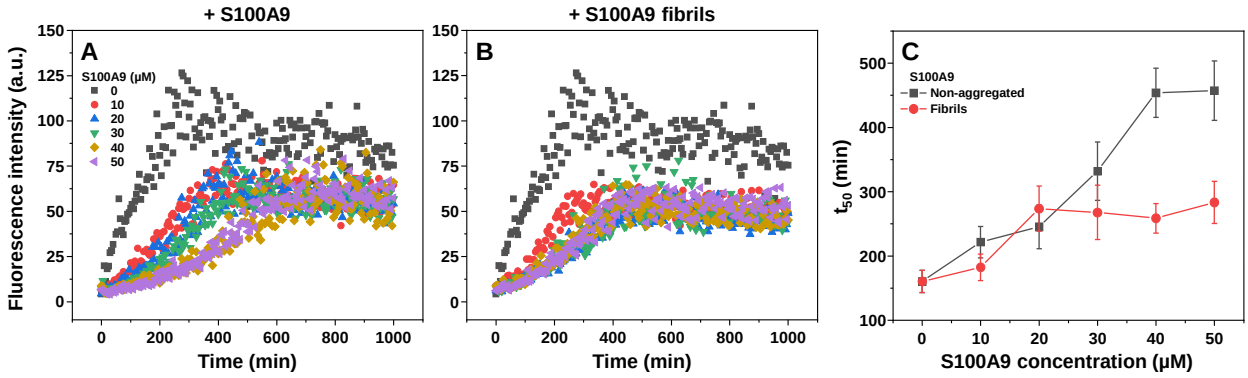


**Figure 4.** Seeded aggregation of prion proteins in the presence of S100A9. Examples of PrP aggregation curves in the presence of different concentrations of non-aggregated S100A9 (A) and S100A9 fibrils (B). Aggregation curve half-time values ($t_{50}$, C). Error bars are for one standard deviation (n=6).

The resulting aggregate samples were then examined by FTIR spectroscopy without any additional reseeding steps. Since S100A9 was shown to not form any detectable amounts of aggregates (Figure 1C), the spectra of samples which contained non-aggregated S100A9 could be compared without any need to account for the protein's presence. In this case, the spectra main maximum was similar for all the samples (1627 – 1628 $cm^{-1}$), while there was a notable difference between the peak sizes associated with beta-sheet hydrogen bonding. There appeared to be a S100A9-concentration-dependent increase in the relative height of the band at 1627-1628 $cm^{-1}$, when compared to the random-coil, alpha-helix and turn/loop regions (1650 – 1680 $cm^{-1}$). These results suggested that S100A9 may have inhibited the self-replication of certain fibril types or promoted the formation of aggregates with larger beta-sheet content in their structure.

FTIR analysis of samples where S100A9 was in its fibrillar state was more complicated, as both protein aggregates were present in the sample. Surprisingly, it was discovered that the spectra from both sets of conditions were comprised of aggregated S100A9, PrP type I (Figure 5A bottom) and type II (Figure 5A top) spectra. This deconvolution procedure (Supplementary Figure S4) revealed that higher concentrations of both types of S100A9 promoted the formation of type II PrP fibrils. In both cases, the 50 µM S100A9 conditions yielded identical PrP fibril secondary structures, regardless whether S100A9 was in its non-aggregated or fibrillar state.

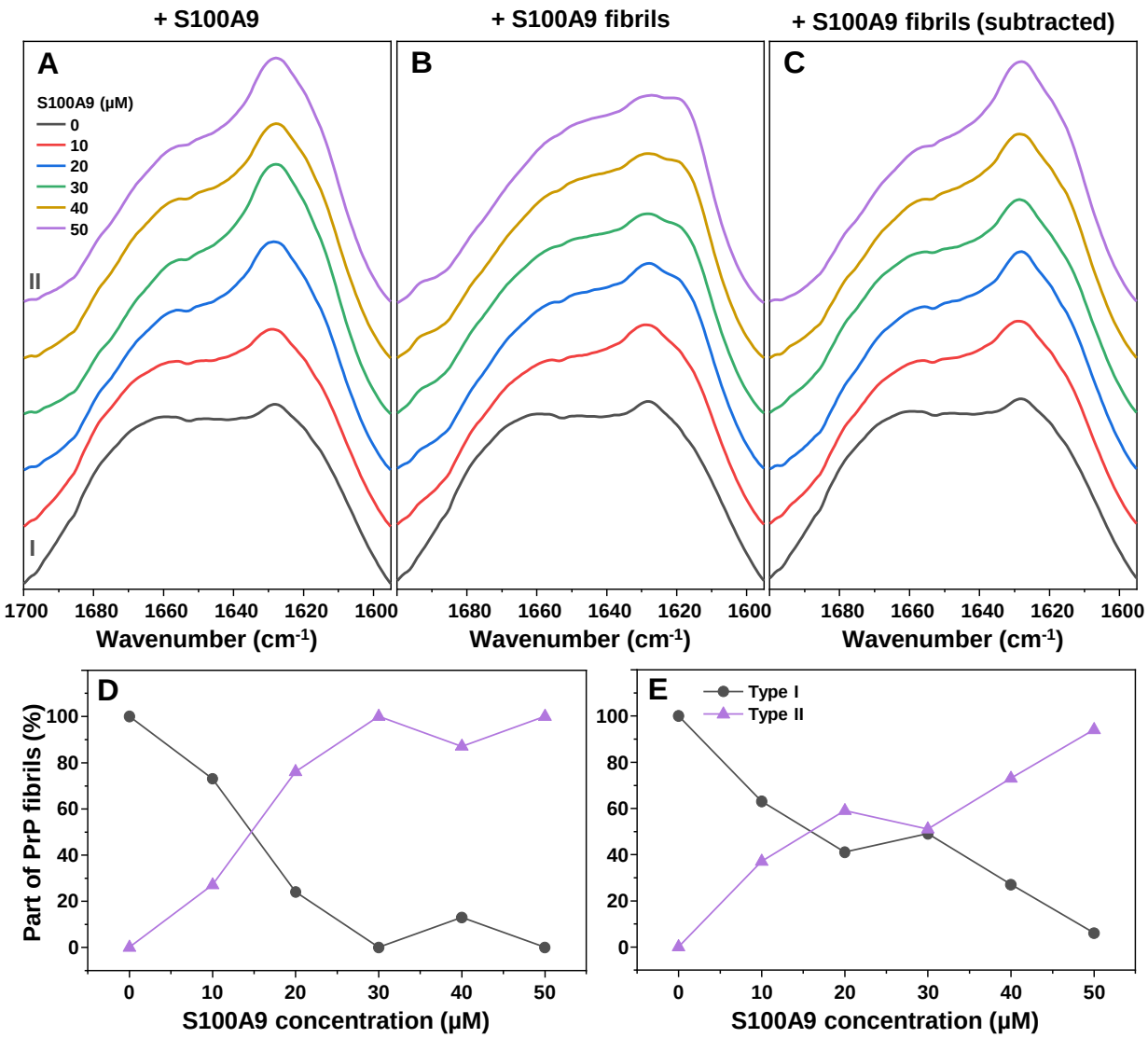


**Figure 5.** Influence of S100A9 on PrP fibril secondary structures during self-replication. Fourier-transform infrared spectra of PrP fibrils after self-replication in the presence of non-aggregated S100A9 (A) and S100A9 fibrils (B). Roman numerals mark type I and type II PrP fibrils. Panel B spectra after S100A9 spectra subtraction (C). FTIR spectra deconvolution results when PrP was replicated in the presence of non-aggregated S100A9 (D) or S100A9 fibrils (E). Deconvolution of each spectrum into the aggregated S100A9 and PrP fibril types I and II is shown as Supplementary Figure S4.

Based on the PrP fibril FTIR spectra in the presence of non-aggregated S100A9 (Figure 5A), there were no detectable signs of association between the two proteins (no appearance of peaks associated with non-aggregated S100A9), suggesting that the interaction may occur with monomeric PrP. During a protein melt assay under 0 M GuHCl conditions, it was observed that both proteins had very similar melting point temperature ($T_m$) values, which made it difficult to distinguish the effect of their cross-interaction (Figure 6A). However, the change in ANS fluorescence intensity when both proteins were in solution together was almost identical to the combined PrP and S100A9 ANS fluorescence intensities (Figure 6B). This result indicated that the presence of S100A9 did not alter the stability of monomeric PrP.

Examination of the samples using size-exclusion chromatography also revealed that there were no notable interactions between the two proteins. The monomeric PrP elution peak (Figure 6C, D) was slightly shifted compared to the combined S100A9-PrP sample peak (10.50 mL and 10.37 mL respectively), indicating that the proteins did not form a complex in solution, or the interaction was transient.

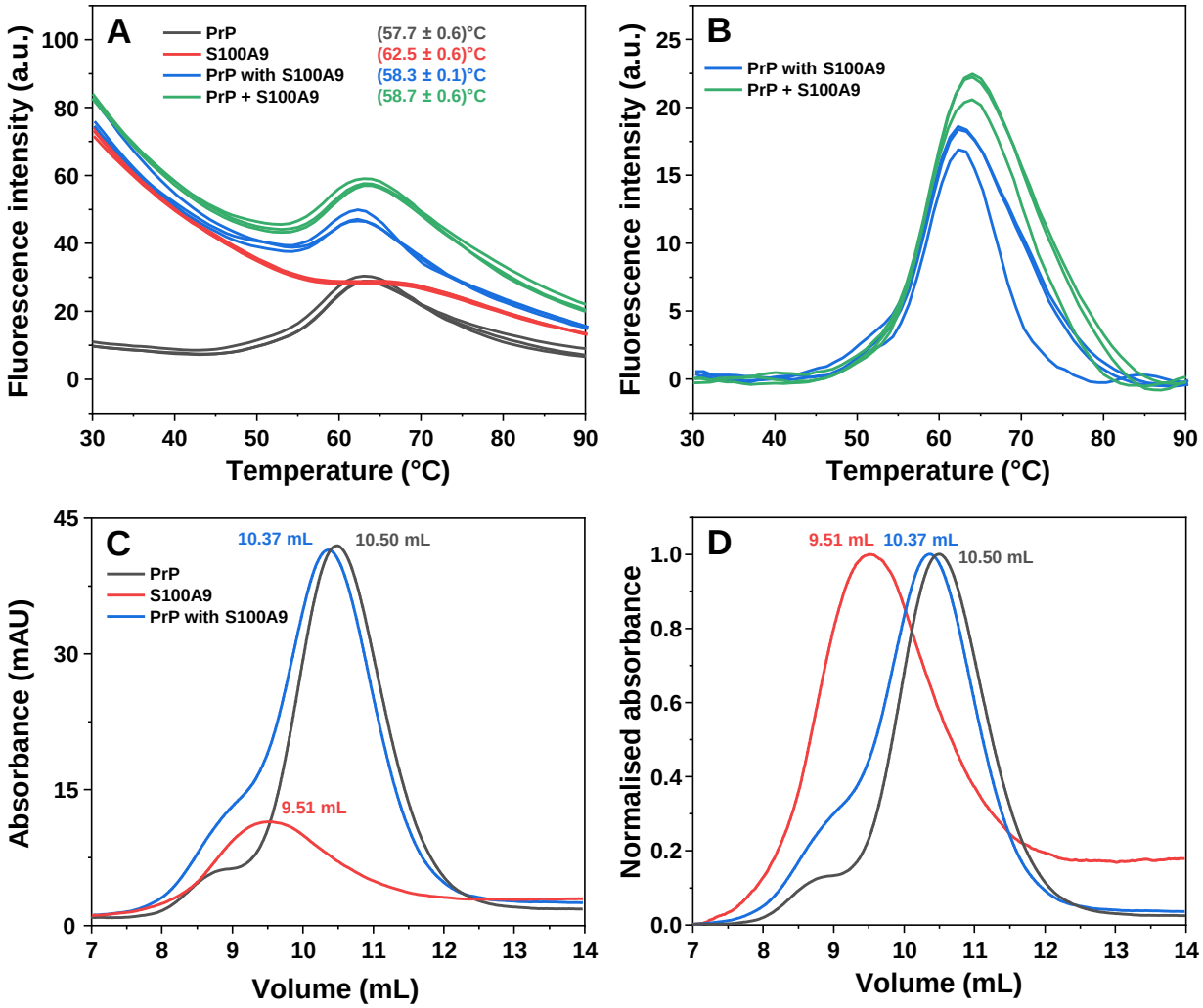


**Figure 6.** Examination of non-aggregated prion protein (PrP) and S100A9 cross-interactions. Protein melt assay of PrP and S100A9 (A, black line – PrP alone, red line – S100A9 alone, blue line – PrP and S100A9 together in solution, green line – combined PrP and S100A9 fluorescence intensities). Fluorescence curve first derivative maximum positions are color-coded and displayed in panel A. Baseline corrected fluorescence intensity dependence on temperature (B). Size-exclusion chromatography elution profiles of PrP (black lines), S100A9 (red lines) and when they are both in solution (blue lines) (C – raw data, D - normalised).

## Discussion

In recent years, there has been a surge in the number of reports describing the cross-interaction of amyloidogenic proteins and how it influences their aggregation process. Both S100A9, as well as prion proteins have previously been shown to participate in these type of interactions [22,28], however, there was lack of information on how they may influence each other's amyloid formation. Since S100A9 is a pro-inflammatory protein, which shares a localisation with PrP [35–37], this work was dedicated to gaining a better understanding of how it can alter the pathway of PrP aggregation *in vitro*.

Based on the non-seeded kinetics of PrP amyloid formation, the non-aggregated S100A9 had a significant inhibitory effect on the primary nucleation phase, while its fibrillar form did not alter the length of the lag phase. This suggests that non-aggregated S100A9 may be capable of disrupting the process of PrP amyloid nuclei formation, either by interacting with monomeric PrP or the prefibrillar structure. Analysis of S100A9 and PrP interactions by size-exclusion chromatography and a protein melt assay did not show any significant signs of complex formation when both proteins were in their native state and their association may have only been transient. Oppositely to the effect on PrP aggregation lag time, the fibrillar form of S100A9 had a significant effect on the process apparent rate constant. This result can be explained by the hydrophobic fibrillar surface of S100A9 acting as a catalyst for surface-mediated nucleation [48]. Such an event may also contribute to the reduction of primary nucleation lag time and compete with the inhibitory effect of S100A9.

The complexity of the study increased when we examined how this cross-interactions affected the self-replication process of PrP fibrils. When the initial PrP aggregates were prepared in the absence of S100A9, they were also only effective at replicating their structure when there was no S100A9 present in the reaction solution. In this case, both the non-aggregated and fibrillar forms of S100A9 significantly increased the process half-time values and changed the PrP aggregation curve shapes from exponential to sigmoidal. The resulting PrP fibril secondary structure also became different than the initial "seed", suggesting that the presence of S100A9 may facilitate the propagation of only certain PrP aggregate types, while inhibiting others. A similar effect was previously observed with alpha-synuclein, where the presence of S100A9 modulated the aggregation reaction and promoted the formation of a single fibril conformation [40].

Further support for the idea of S100A9 selectively altering the amyloid formation of PrP could be obtained by analysing the PrP fibril structures generated during spontaneous aggregation. When the reaction solutions contained a small concentration of S100A9, some of the samples resulted in FTIR spectra similar to the ones observed in the self-replication experiment. At higher S100A9 concentrations, the PrP fibril FTIR spectra became completely different from the controls, while being nearly identical between non-aggregated and fibrillar S100A9 conditions. In our previous examination of PrP and superoxide dismutase-1 (SOD1) cross-interaction, similar FTIR spectra were also observed when PrP was aggregated in the presence of SOD1 [39]. Under 50 µM SOD1 conditions, however, the FTIR spectra were completely different from the ones observed under 50 µM S100A9 conditions, indicating that different amyloidogenic proteins may have distinct effects on PrP aggregation.

Another peculiar aspect was the difference between the secondary structure of PrP aggregates depending on whether they initially formed in the presence of S100A9 or were only replicated with S100A9. This observation implies that the cross-interaction promotes the formation of certain PrP

amyloid nuclei, which can effectively replicate under conditions with S100A9. However, if the reaction solution is “seeded” with preformed PrP aggregates, S100A9 inhibits their elongation or only facilitates the replication of specific fibril types. These results further support the idea that S100A9 interacts with the aggregation centers of PrP, whether they are the prefibrillar nuclei or the elongation-competent ends of fibrils. Interactions with only these specific structures would explain why we did not observe any significant signs of S100A9 association with either monomeric or aggregated PrP.

The results of this study demonstrate the highly complex cross-interaction between the proinflammatory S100A9 and prion proteins during amyloid aggregation. S100A9 is capable of altering both the kinetic parameters of PrP fibril formation, as well as their resulting secondary structure and self-replication properties. Taking into consideration the shared localisation with PrP and previous reports of possible S100A9 involvement in neurodegenerative disorders, this study adds another piece to the complex amyloid interactome puzzle.

**Author Contributions:** Conceptualization, M.Z. and V.S.; investigation, M.Z., D.S., K.M. and A.S.; resources, V.S.; data analysis, M.Z., D.S. and V.S.; writing—original draft preparation, M.Z.; writing—review and editing, M.Z., D.S., K.M., A.S. and V.S. All authors have read and agreed to the published version of the manuscript.

**Funding:** This research was funded by the Research Council of Lithuania, grant number S-MIP-22-34.

**Data Availability Statement:** All data are available in the Mendeley data online repository: https://data.mendeley.com/datasets/8t7hxxnc53/1

**Conflicts of Interest:** The authors declare no conflict of interest.

**References**


1. Chiti, F. & Dobson, C. M. Protein Misfolding, Amyloid Formation, and Human Disease: A Summary of Progress Over the Last Decade. *Annu. Rev. Biochem.* **86**, 27–68 (2017).

2. Knowles, T. P. J., Vendruscolo, M. & Dobson, C. M. The amyloid state and its association with protein misfolding diseases. *Nat. Rev. Mol. Cell Biol.* **15**, 384–396 (2014).

3. Sinsky, J., Pichlerova, K. & Hanes, J. Tau Protein Interaction Partners and Their Roles in Alzheimer's Disease and Other Tauopathies. *Int. J. Mol. Sci.* **22**, 9207 (2021).

4. Mehra, S., Gadhe, L., Bera, R., Sawner, A. S. & Maji, S. K. Structural and functional insights into α-synuclein fibril polymorphism. *Biomolecules* **11**, (2021).

5. d'Errico, P. & Meyer-Luehmann, M. Mechanisms of Pathogenic Tau and Aβ Protein Spreading in Alzheimer's Disease. *Front. Aging Neurosci.* **12**, 1–10 (2020).

6. Cummings, J. *et al.* Alzheimer's disease drug development pipeline: 2023. *Alzheimer's Dement. Transl. Res. Clin. Interv.* **9**, (2023).

7. Mehta, D., Jackson, R., Paul, G., Shi, J. & Sabbagh, M. Why do trials for Alzheimer's disease drugs keep failing? A discontinued drug perspective for 2010-2015. *Expert Opin. Investig. Drugs* **26**, 735–739 (2017).

8. Arthur, K. C. *et al.* Projected increase in amyotrophic lateral sclerosis from 2015 to 2040. *Nat. Commun.* **7**, 12408 (2016).

9. Brookmeyer, R., Gray, S. & Kawas, C. Projections of Alzheimer's disease in the United States and the public health impact of delaying disease onset. *Am. J. Public Health* **88**, 1337–1342 (1998).

10. Meisl, G. *et al.* Molecular mechanisms of protein aggregation from global fitting of kinetic models. *Nat. Protoc.* **11**, 252–272 (2016).

11. Meisl, G. *et al.* Differences in nucleation behavior underlie the contrasting aggregation kinetics of the Aβ40 and Aβ42 peptides. *Proc. Natl. Acad. Sci.* **111**, 9384–9389 (2014).

12. Buell, A. K. *et al.* Solution conditions determine the relative importance of nucleation and growth processes in  -synuclein aggregation. *Proc. Natl. Acad. Sci.* **111**, 7671–7676 (2014).

13. Gurry, T. & Stultz, C. M. Mechanism of amyloid-β fibril elongation. *Biochemistry* **53**, 6981–6991 (2014).

14. Rodriguez, R. A., Chen, L. Y., Plascencia-Villa, G. & Perry, G. Thermodynamics of Amyloid-β Fibril Elongation: Atomistic Details of the Transition State. *ACS Chem. Neurosci.* **9**, 783–789 (2018).

15. Nicoud, L., Lazzari, S., Balderas Barragán, D. & Morbidelli, M. Fragmentation of Amyloid Fibrils Occurs in Preferential Positions Depending on the Environmental Conditions. *J. Phys. Chem. B* **119**, 4644–4652 (2015).

16. Törnquist, M. *et al.* Secondary nucleation in amyloid formation. *Chem. Commun.* **54**, 8667–8684 (2018).

17. Gaspar, R. *et al.* Secondary nucleation of monomers on fibril surface dominates α-synuclein aggregation and provides autocatalytic amyloid amplification. *Q. Rev. Biophys.* **50**, (2017).

18. Wiśniewski, J. R., Hein, M. Y., Cox, J. & Mann, M. A 'proteomic ruler' for protein copy number and concentration estimation without spike-in standards. *Mol. Cell. Proteomics* **13**, 3497–3506 (2014).

19. Ono, K., Takahashi, R., Ikeda, T. & Yamada, M. Cross-seeding effects of amyloid β-protein and α-synuclein. *J. Neurochem.* **122**, 883–890 (2012).

20. Vasconcelos, B. *et al.* Heterotypic seeding of Tau fibrillization by pre-aggregated Abeta provides potent seeds for prion-like seeding and propagation of Tau-pathology in vivo. *Acta Neuropathol.* **131**, 549–569 (2016).

21. Nisbet, R. M., Polanco, J.-C., Ittner, L. M. & Götz, J. Tau aggregation and its interplay with amyloid-β. *Acta Neuropathol.* **129**, 207–220 (2015).

22. Honda, R. Amyloid-β Peptide Induces Prion Protein Amyloid Formation: Evidence for Its Widespread Amyloidogenic Effect. *Angew. Chemie - Int. Ed.* **57**, 6086–6089 (2018).

23. Guo, J. L. *et al.* Distinct α-Synuclein Strains Differentially Promote Tau Inclusions in Neurons. *Cell* **154**, 103–117 (2013).

24. Lu, J. *et al.* Structural basis of the interplay between α-synuclein and Tau in regulating pathological amyloid aggregation. *J. Biol. Chem.* **295**, 7470–7480 (2020).

25. Katorcha, E. *et al.* Cross-seeding of prions by aggregated α-synuclein leads to transmissible spongiform encephalopathy. *PLoS Pathog.* **13**, 1–23 (2017).

26. Vogl, T., Gharibyan, A. L. & Morozova-Roche, L. A. Pro-inflammatory S100A8 and S100A9 proteins: Self-assembly into multifunctional native and amyloid complexes. *Int. J. Mol. Sci.* **13**, 2893–2917 (2012).

27. Wang, C. *et al.* The role of pro-inflammatory S100A9 in Alzheimer's disease amyloid-neuroinflammatory cascade. *Acta Neuropathol.* **127**, 507–522 (2014).

28. Horvath, I. *et al.* Co-aggregation of pro-inflammatory S100A9 with α-synuclein in Parkinson's disease: ex vivo and in vitro studies. *J. Neuroinflammation* **15**, 172 (2018).

29. Esposito, G. *et al.* S100B induces tau protein hyperphosphorylation via Dickopff-1 up-regulation and disrupts the Wnt pathway in human neural stem cells. *J. Cell. Mol. Med.* **12**, 914–927 (2008).

30. Linden, R. The biological function of the prion protein: A cell surface scaffold of signaling modules. *Front. Mol. Neurosci.* **10**, 1–19 (2017).

31. Collinge, J. Variant Creutzfeldt-Jakob disease. *Lancet* **354**, 317–323 (1999).

32. Baldwin, K. J. & Correll, C. M. Prion Disease. *Semin. Neurol.* **39**, 428–439 (2019).

33. Caughey, B. & Chesebro, B. Transmissible spongiform encephalopathies and prion protein interconversions. *Adv. Virus Res.* **56**, (2001).

34. Wang, M., Herrmann, C. J., Simonovic, M., Szklarczyk, D. & von Mering, C. Version 4.0 of PaxDb: Protein abundance data, integrated across model organisms, tissues, and cell-lines. *Proteomics* **15**, 3163–3168 (2015).

35. Kim, M.-S. *et al.* A draft map of the human proteome. *Nature* **509**, 575–581 (2014).

36. Bauernfeind, A. L. *et al.* High spatial resolution proteomic comparison of the brain in humans and chimpanzees. *J. Comp. Neurol.* **523**, 2043–2061 (2015).

37. Guldbrandsen, A. *et al.* In-depth Characterization of the Cerebrospinal Fluid (CSF) Proteome Displayed Through the CSF Proteome Resource (CSF-PR). *Mol. Cell. Proteomics* **13**, 3152–3163 (2014).

38. Li, B., Chen, M. & Zhu, C. Neuroinflammation in Prion Disease. *Int. J. Mol. Sci.* **22**, 2196 (2021).

39. Ziaunys, M., Mikalauskaite, K., Veiveris, D., Sakalauskas, A. & Smirnovas, V. Superoxide dismutase-1 alters the rate of prion protein aggregation and resulting fibril conformation. *Arch. Biochem. Biophys.* **715**, 109096 (2022).

40. Toleikis, Z. *et al.* S100A9 Alters the Pathway of Alpha-Synuclein Amyloid Aggregation. *Int. J. Mol. Sci.* **22**, 7972 (2021).

41. Milto, K., Michailova, K. & Smirnovas, V. Elongation of Mouse Prion Protein Amyloid-Like Fibrils: Effect of Temperature and Denaturant Concentration. *PLoS One* **9**, e94469 (2014).

42. Mikalauskaite, K., Ziaunys, M., Sneideris, T. & Smirnovas, V. Effect of Ionic Strength on Thioflavin-T Affinity to Amyloid Fibrils and Its Fluorescence Intensity. *Int. J. Mol. Sci.* **21**, 8916 (2020).

43. Mikalauskaite, K., Ziaunys, M. & Smirnovas, V. Lysozyme Amyloid Fibril Structural Variability Dependence on Initial Protein Folding State. *Int. J. Mol. Sci.* **23**, 5421 (2022).

44. Foderà, V. *et al.* Thioflavin T Hydroxylation at Basic pH and Its Effect on Amyloid Fibril Detection. *J. Phys. Chem. B* **112**, 15174–15181 (2008).

45. Barth, A. Infrared spectroscopy of proteins. *Biochim. Biophys. Acta - Bioenerg.* **1767**, 1073–1101 (2007).

46. Pansieri, J. *et al.* Templating S100A9 amyloids on Aβ fibrillar surfaces revealed by charge detection mass spectrometry, microscopy, kinetic and microfluidic analyses. *Chem. Sci.* **11**, 7031–7039 (2020).

47. Ziaunys, M., Sneideris, T. & Smirnovas, V. Formation of distinct prion protein amyloid fibrils under identical experimental conditions. *Sci. Rep.* **10**, 4572 (2020).

48. Koloteva-Levine, N. *et al.* Amyloid particles facilitate surface-catalyzed cross-seeding by acting as promiscuous nanoparticles. *Proc. Natl. Acad. Sci. U. S. A.* **118**, 1–12 (2021).